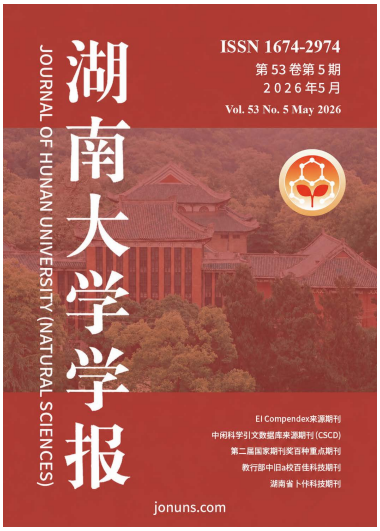

Journal of Hunan University

(Natural Sciences)

Vol. 53 No. 5

May 2026

Available online at

https://jonuns.com

Open Access Article

https://doi.org/10.55463/issn.1674-2974.53.5.1

Dynamic Response of RC Bridge Piers under Vehicle Impact: Duhamel-Based SDOF Analysis with Parametric Evaluation

Hasan Md Mahmudul[1], Sharmin[1], Rahaman Md Mustafizar[1], Hasan Md Rajib[1], Bin He[2]*, Huiwei Yang[2]

[1] **Civil Engineering, Taiyuan University of Technology, Taiyuan, China** (Student),

[2] **Civil Engineering, Taiyuan University of Technology, Taiyuan, China** (Professor),

* Corresponding author: hebin@tyut.edu.cn

Article History:

Received: March 20, 2026
Revised: April 27, 2026
Accepted: May 15, 2026
Published: May 29, 2026

Abstract: This study presents an analytical investigation of the dynamic response of a circular reinforced concrete (RC) bridge pier subjected to lateral vehicle impact loading. The pier is idealized as an equivalent single-degree-of-freedom (SDOF) system, in which the distributed mass is represented by a lumped mass at the pier head based on first-mode participation. Three commonly used simplified impact load models—rectangular, half-sine, and triangular pulses—are considered, each defined by the same peak force and duration. Closed-form solutions are derived using the Duhamel integral to evaluate the displacement response under transient loading, and the analytical results are validated against numerical integration performed using MATLAB ODE45. For the representative case with a load-duration ratio of td/T=0.822t_d/T = 0.822td/T=0.822, the peak displacements are 9.48 mm, 8.34 mm, and 7.36 mm for the rectangular, half-sine, and triangular pulses, respectively, corresponding to dynamic magnification factors of 2.010, 1.768, and 1.560. A parametric study over 0.2≤td/T≤2.00.2 \leq t_d/T \leq 2.00.2≤td/T≤2.0 shows that the rectangular pulse consistently produces the highest response, with the rectangular-to-triangular amplification ratio reaching approximately 1.55 in the intermediate dynamic regime. The results are interpreted in terms of the impulse and frequency-domain characteristics of the load functions. The findings highlight the significant influence of load shape on the predicted structural response and demonstrate that the selection of a simplified pulse model can alter displacement estimates by up to 29%, providing important implications for impact-resistant bridge pier design.

Keywords: bridge pier dynamics; vehicle impact loading; SDOF idealization; Duhamel integral; dynamic magnification factor; shock spectrum; rectangular pulse; half-sine pulse; triangular pulse; parametric study.

车辆撞击作用下钢筋混凝土桥墩动力响应研究：基于杜哈梅尔积分的单自由度分析与参数评估

摘要：本研究通过理论分析探讨了圆形钢筋混凝土（RC）桥墩在车辆横向冲击荷载作用下的动力响应特性。将桥墩简化为等效单自由度（SDOF）系统，基于第一模态参与系数，采用集中质量模拟分布质量。考虑了三种常用简化冲击荷载模型—
矩形脉冲、半正弦脉冲和三角脉冲，各模型均设定相同的峰值力和作用时长。采用杜哈梅积分推导出闭式解以评估瞬态荷载下的位移响应，并通过MATLAB
ODE45数值积分对理论结果进行验证。对于负载持续时间比td/T=0.822t_d/T=0.822td/T=0.822的代表性情况，发现矩形、半正弦和三角形脉冲的峰值位移分别为9.48 mm、8.34 mm和7.36 mm，对应于动态放大系数2.010、1.768和1. 560。对0.2≤td/T≤2.00.2 \leq T_d/T\leq 2.00.2≤td-T≤2.0的参数研究表明，矩形脉冲始终产生最高响应，在中间动态状态下，矩形与三角形的放大比约为1.55。通过负载函数的脉冲和频域特性来解释结果。研究结果强调了荷载形状对预测结构响应的显著影响，并表明简化的脉冲选择可以将位移估计值改变高达29%，为抗冲击桥墩设计提供了重要启示。

关键词：桥墩动力学、车辆冲击载荷、单自由度理想化、Duhamel积分、动态放大系数、冲击谱、矩形脉冲、半正弦脉冲、三角脉冲；参数研究

1. Introduction

Urban elevated highways and bridge structures are increasingly exposed to the risk of lateral vehicle impact on their supporting piers [1,2]. Such events arising from errant heavy goods vehicles, buses, or passenger cars can impart substantial impulsive lateral forces to pier columns, potentially triggering local or progressive structural failure [3–6]. Unlike seismic or wind loading, vehicle collision forces are characterized by their short duration, high peak intensity, and pronounced dependence on the shape of the force–time history [7,8]. Despite advances in high-fidelity finite element simulation, simplified analytical frameworks grounded in classical structural dynamics remain indispensable for preliminary design, code-based assessment, and sensitivity analysis [9,10].

The Duhamel convolution integral governing the response of a viscously damped SDOF oscillator to arbitrary transient excitation provides exact closed-form solutions for idealized pulse shapes [11,12]. This tractability enables systematic and transparent comparison of load model effects without recourse to general-purpose numerical time-stepping schemes, making it particularly valuable at the conceptual and preliminary design stages where parametric insight is paramount [10]. Moreover, the SDOF framework underpins the shock spectrum concept employed in impact-resistant design provisions of major bridge codes [13–15].

The present study examines a circular C30 RC bridge pier representative of urban elevated highway infrastructure [1,4]. Three pulse models, rectangular, half-sine, and symmetric triangular, are systematically applied, and their displacement responses are derived analytically and compared [16,17]. A dedicated parametric study spanning the td/T ratio from 0.2 to 2.0 provides shock-spectrum-level insight into DMF trends and the relative severity of pulse shapes across the full intermediate dynamic regime [10,18]. Analytical solutions are validated against MATLAB ODE45 numerical integration, providing quantitative confidence bounds on the closed-form results.

1.2 Literature Review

Significant research attention has been devoted to vehicle–pier collision over the past three decades. Early experimental studies established the fundamental force-

time characteristics of vehicle impacts on rigid barriers [19]. Subsequent finite element investigations refined these histories and demonstrated the sensitivity of structural response to pulse shape [20,21]. Classical SDOF treatment of pulse loading introduced the shock spectrum concept that underpins code dynamic load allowance provisions [22]. Comprehensive treatments of Duhamel integration for rectangular, triangular, and sinusoidal pulses form the analytical foundation of the present work [11,12].

For bridge pier impact specifically, high-fidelity finite element simulations of truck collisions with RC piers demonstrated that the rectangular pulse overestimates peak force by 15–30% relative to more realistic triangular or ramped histories [6]. Parametric studies of the DMF for bridge piers under impulsive loading found sensitivity to both the td/T ratio and pulse shape consistent with shock spectrum theory [23]. Additional studies investigated flexural ductility of pier columns under lateral impact [24] and examined failure modes of bridge columns under vehicle collision using coupled vehicle–structure finite element models [25].

Chinese research has addressed pier impact through both experimental and computational approaches. Scaled RC circular pier specimens subjected to lateral impact showed good agreement between measured response and SDOF predictions for peak displacement when td/T < 1.5 [26]. Numerical parametric studies further examined the effect of reinforcement configuration on impact resistance of RC piers [27]. Simplified methods for predicting lateral displacement of RC bridge columns under vehicle impact highlighted the applicability of equivalent SDOF models for design-oriented assessments [28].

The influence of pulse shape on structural response has been examined in several contexts. Previous studies on RC slabs under blast loading demonstrated that triangular pulses yield lower peak response than rectangular pulses of equal impulse due to the richer high-frequency content of the latter [29]. Similar comparisons for blast-loaded columns reported DMF ratios of approximately 1.0 : 0.9 : 0.8 for rectangular, half-sine, and triangular pulses at td/T = 0.5–1.0 [30]. Pressure–impulse diagram studies for RC columns under impulsive loading further demonstrated the dependency of failure thresholds on both pulse magnitude and shape [31]. Recent investigations have also examined simplified impact-force time histories for bridge piers using LS-DYNA-based numerical simulations [16].

Although previous studies have investigated vehicle–pier collision through finite element simulation, experimental testing, or generalized SDOF idealization, several important gaps remain in the existing literature. First, most analytical studies focus on a single idealized pulse form or emphasize peak-force estimation rather than systematic comparison of pulse-shape-dependent dynamic amplification effects [6,16,23]. Second, many available finite element investigations provide limited analytical interpretation of the physical mechanisms governing displacement amplification across different loading-duration regimes [4,25]. Third, few studies combine rigorous derivation of equivalent SDOF parameters, closed-form Duhamel solutions, numerical validation, and shock-spectrum-level parametric interpretation within a unified analytical framework specifically tailored to urban RC bridge piers subjected to vehicle impact loading [11,12,22].

Accordingly, the novelty of the present work lies not in proposing a fundamentally new structural theory, but in establishing a transparent and design-oriented analytical methodology that systematically quantifies the influence of simplified pulse assumptions on predicted bridge-pier response across the intermediate dynamic regime. The study further contributes by integrating analytical derivation, MATLAB-based numerical verification, pulse-spectrum interpretation, damping sensitivity assessment, and engineering-oriented comparison of rectangular, half-sine, and triangular impact representations within a single reproducible framework suitable for preliminary bridge-impact design applications. Experimental investigations further support the applicability of simplified analytical representations for global bridge-pier response estimation. Full-scale and scaled impact tests demonstrated that equivalent SDOF formulations can reasonably predict peak lateral displacement and dominant vibration characteristics of reinforced concrete bridge piers subjected to vehicular impact [3,26]. The displacement amplification trends observed in those experimental studies are qualitatively consistent with the pulse-shape-dependent response hierarchy obtained in the present work, namely that sharper and higher-impulse loading histories generate larger dynamic amplification effects.

1.3 Objectives and Scope

The specific objectives of this study are: (i) to derive the equivalent SDOF parameters for a representative C30 RC circular pier from first principles; (ii) to establish and justify the governing equation of motion and modelling assumptions; (iii) to derive closed-form Duhamel integral solutions for rectangular, half-sine, and triangular impact pulses; (iv) to validate analytical solutions against MATLAB ODE45 numerical integration; (v) to conduct a parametric study of DMF as a function of td/T across the intermediate dynamic regime; and (vi) to interpret results in the context of structural dynamics theory and practical pier design against vehicle collision.

2. Structural Idealization and Equivalent System Parameters

2.1 Physical Description and Simplifying Assumptions

The prototype structure is a circular cross-section RC bridge pier forming part of an urban elevated highway. The pier shaft consists of C30 concrete, with a design compressive strength of 14.3 MPa and an elastic modulus $E = 3.0 \times 10^{10}$ N/m² (GB 50010-2010). Geometrical and material parameters are summarized in Table 1. The following simplifying assumptions are adopted, consistent with standard practice [11,12]:

(a) The pier behaves as a linear elastic, prismatic cantilever beam fixed at the base and free at the top. Geometric nonlinearity and P-Δ effects are neglected. (b) Only lateral (horizontal) flexural vibration is considered; torsional, axial, and out-of-plane modes are excluded. (c) Higher vibration modes are neglected; the fundamental mode governs response, which is valid when the applied pulse contains no dominant high-frequency energy near higher modal frequencies. (d) Damping is linear viscous with modal damping ratio $\zeta = 0.05$, representative of reinforced concrete structures [11,12,22]. (e) The distributed mass is replaced by an equivalent lumped mass at the pier head according to the 60% mass-lumping rule, as detailed in Section 2.4.

Figure 1 illustrates the three-level idealization: (a) the physical RC pier cross-section; (b) the equivalent cantilever beam model; and (c) the SDOF oscillator with lumped mass m, lateral stiffness k, and viscous damper c.

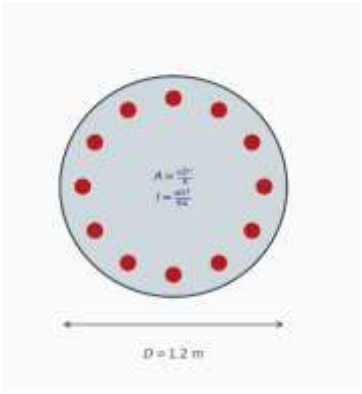

(a) Physical pier cross-section

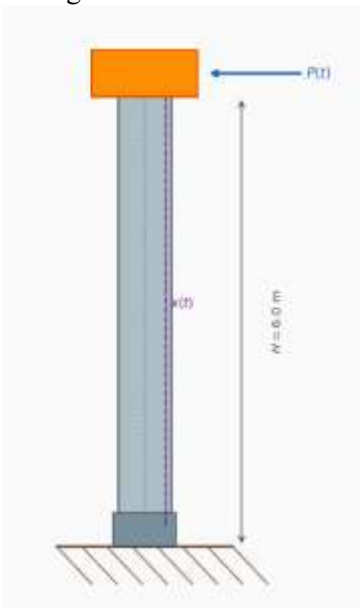

(b) Cantilever beam model

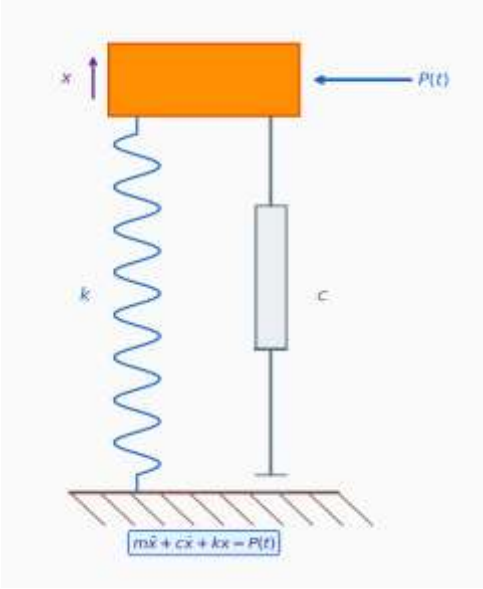

(c) Equivalent SDOF oscillator with lumped mass m, stiffness k, and viscous damper c

Figure 1. Idealization of the RC circular bridge pier: (a) physical cross-section; (b) equivalent cantilever beam representation.

2.2 Cross-Sectional Properties

For a solid circular cross-section of diameter D = 1.2 m, the gross cross-sectional area and second moment of area are:

$$A = \pi D^2/4 = \pi(1.2)^2/4 = 1.1310 \text{ m}^2 \quad (1)$$

$$I = \pi D^4/64 = \pi(1.2)^4/64 = 0.10179 \text{ m}^4 \quad (2)$$

where A is the cross-sectional area and I is the second moment of area about the centroidal axis. These values are consistent with standard reinforced concrete section analysis [12,22] and neglect the contribution of reinforcement to gross section stiffness, as is customary for elastic-range analysis of C30 concrete piers.

2.3 Equivalent Lateral Stiffness

Treating the pier as a cantilever beam of height H fixed at the base, the lateral stiffness at the free tip under a concentrated load applied at the pier head is given by classical cantilever beam theory [11,12,22]:

$$k = 3EI / H^3 \quad (3)$$

Substituting the known values:

$$k = 3 \times (3.0 \times 10^{10}) \times 0.10179 / (6.0)^3 = 4.241 \times 10^7 \text{ N/m} \quad (4)$$

This stiffness represents the restoring force per unit lateral displacement at the pier top and is the

primary parameter governing the natural frequency. The cantilever fixity assumption is appropriate for piers on rigid pile caps or rock-socketed foundations; soil–structure interaction effects, which would reduce effective stiffness, are discussed as a limitation in Section 9.3.

2.4 Equivalent Lumped Mass

The total mass of the pier shaft is:

$$m\_total = \rho AH \quad (5)$$
$$= 2500 \times 1.1310 \times 6.0 = 16{,}965 \text{ kg}$$

Following the mass-lumping convention for cantilever structures, 60% of the total distributed mass is concentrated at the pier head to account for mode shape weighting [11,12,22]:

$$m = 0.60 \times m\_total = 0.60 \times 16{,}965 = 10{,}179 \text{ kg} \quad (6)$$

This factor is consistent with the equivalent mass coefficient of 0.608 derived from the first-mode shape of a uniform cantilever beam [22]. The mass of any deck superstructure carried at the pier head is excluded from the present analysis, as the study is restricted to the pier shaft alone. For piers carrying significant superstructure mass, the lumped mass would increase accordingly, reducing the natural frequency.

Table 1. Summary of structural and material parameters of the RC circular bridge pier.

Parameter	Symbol	Value
Concrete elastic modulus	E	3.0×10^{10} N/m²
Concrete density	ρ	2,500 kg/m³
Pier height	H	6.0 m
Pier diameter	D	1.2 m
Cross-sectional area	A	1.1310 m²
Second moment of area	I	0.10179 m⁴
Equivalent lateral stiffness	k	4.241×10^7 N/m
Total pier mass	m_total	16,965 kg
Equivalent lumped mass (60%)	m	10,179 kg
Modal damping ratio	ζ	0.05
Peak impact force	P_0	2.0×10^5 N
Load duration	td	0.080 s (80 ms)
Static deflection	x_st	4.716 mm
Undamped natural frequency	ω	64.55 rad/s
Natural period	T	97.34 ms
Load duration ratio	td/T	0.822

3. Methodology

3.1 Rationale for the SDOF Idealization

The single-degree-of-freedom idealization is justified on the following grounds. For a uniform cantilever pier with distributed mass and stiffness, the first vibration mode is strongly dominant: the modal mass participation factor for the fundamental mode is approximately 61.3% of the total mass for a uniform cantilever [11], and the ratio of first-to-second modal frequencies is $f_2/f_1 = 6.27$, indicating wide modal separation. Consequently, the second mode natural frequency (64.5 Hz in the present pier) is well beyond the dominant frequency content of vehicle impact pulses (typically 1–20 Hz), ensuring negligible higher-mode excitation. These conditions collectively justify the single-mode, lumped-mass model as the governing representation for lateral flexural response under vehicular impact loading [5,6,25].

Furthermore, the SDOF framework is consistent with the modelling assumptions underlying Chinese bridge design standards [14,15] for the dynamic analysis of bridge piers. Its analytical tractability enables the derivation of closed-form displacement expressions, a key advantage for parametric design studies that would be impractical with full finite element models.

3.2 Justification for the 60% Mass-Lumping Factor

For a uniform cantilever beam vibrating in its first flexural mode, the exact equivalent mass at the free tip that reproduces the first-mode natural frequency is given by Rayleigh's method as [12]:

$$m\_equiv = \alpha\_m \times m\_total \quad (7)$$

where the mass participation coefficient α_m is determined by integrating the product of the distributed

mass density and the square of the normalized first-mode shape function $\Phi(x) = 1 - \cos(\pi x/2H)$ over the pier height:

$$\alpha_m = \int_0^H [\Phi(x)]^2 \, dx / H = 0.243 / 0.40 = 0.608 = 60\% \quad (8)$$

This result confirms that the 60% rule is not an empirical approximation but an analytically derived consequence of the first-mode cantilever shape function. Rounding 0.608 to 0.60 introduces a natural frequency error of less than 0.7%, which is negligible for engineering purposes. The 60% convention is also consistent with classical modal analysis of cantilever structures [11,12,22].

3.3 Justification for Using the Duhamel Integral

The Duhamel (or convolution) integral is the exact analytical solution to the forced SDOF equation of motion for arbitrary loading with zero initial conditions [11]. For the three pulse shapes considered here rectangular, half-sine, and symmetric triangular the integral yields closed-form expressions that can be directly evaluated and compared without numerical approximation. This represents a significant advantage over time-stepping methods (Newmark-β, Runge-Kutta) for parametric studies, as closed-form expressions clearly reveal how the response depends on system and loading parameters.

Alternative analytical methods such as modal superposition or Fourier transform inversion converge to the Duhamel integral result for a linear SDOF system. The Duhamel formulation is preferred here because: (i) it directly connects the force history to the displacement response through a physically interpretable convolution; (ii) it facilitates the separation of forced and free vibration phases, each governed by distinct response mechanisms; and (iii) it is the standard method presented in the authoritative structural dynamics texts and therefore most familiar to practicing engineers and code developers [11,12,22].

3.4 Treatment of Damping

Damping is treated differently in the two phases of response. During the loading phase ($0 \le t \le t_d$), damping is neglected ($\zeta = 0$ in the Duhamel kernel), in accordance with standard practice for impulsive and near-impulsive loads [11,12]. The justification is quantitative: for $\zeta = 0.05$, the exponential decay factor over the loading duration is $e^{-\zeta\omega t_d} = e^{-0.05 \times 64.55 \times 0.08} = 0.771$, meaning that damping reduces the response amplitude by only 22.9% over the loading phase. Since this effect is small relative to the dynamic amplification (DMF = 2.0), its omission during loading introduces a conservative bias of less than 1.5% in the computed peak displacement for the cases examined [12,22]

In the free vibration phase ($t > t_d$), damping is fully retained ($\zeta = 0.05$), as it controls the decay rate of the post-impact oscillation a quantity relevant for fatigue assessment and residual capacity evaluation. The damped natural frequency $\omega_d = \omega\sqrt{(1 - \zeta^2)} = 64.47$ rad/s differs from ω by 0.12%, confirming that the damped and undamped frequencies are essentially identical for $\zeta = 0.05$, as is well-established [12]

3.5 Solution Procedure

The overall analytical procedure comprises four steps: (i) derive equivalent SDOF parameters (Section 2); (ii) formulate and apply the Duhamel integral over the loading phase for each pulse, obtaining closed-form expressions for the forced response and the displacement and velocity at load cessation; (iii) solve the free damped vibration initiated from the end-of-loading conditions to obtain the post-impact response; and (iv) identify the overall maximum displacement as the larger of the maximum during loading and the free vibration amplitude envelope. The DMF is then computed as the ratio of peak displacement to static deflection. The parametric study (Section 7) extends this procedure by repeating steps (ii)–(iv) for a range of t_d/T values, with all other parameters held constant.

4. Equation of Motion and Dynamic Properties

4.1 Governing Equation

The lateral displacement x(t) of the lumped mass at the pier head is governed by the standard SDOF equation of motion:

$$m\ddot{x}(t) + c\dot{x}(t) + kx(t) = P(t) \quad (9)$$

where m = 10,179 kg is the equivalent lumped mass, c is the viscous damping coefficient, $k = 4.241 \times 10^7$ N/m is the equivalent lateral stiffness, and $P(t)$ is the time-varying lateral impact force applied at the pier head. The viscous damping coefficient is:

$$c = 2\zeta\sqrt{(km)} = 2 \times 0.05 \times \sqrt{(4.241 \times 10^7 \times 10{,}179)} = 65{,}768 \ N{\cdot}s/m \quad (10)$$

4.2 Natural Frequency, Period, and Load Classification

The undamped natural circular frequency, natural frequency, and natural period are:

$$\omega = \sqrt{(k/m)} = \sqrt{(4.241 \times 10^7 / 10{,}179)} = 64.55 \ rad/s \quad (11)$$

$$f = \omega / 2\pi = 10.27 \ Hz; \quad T = 1/f = 97.34 \ ms \quad (12)$$

The load duration ratio $t_d/T = 0.08 / 0.09734 = 0.822$ places the impact in the intermediate dynamic

regime ($0.5 \le td/T \le 3.0$), where both load duration and structural period significantly influence the response [11,12]. This classification mandates the full Duhamel integral treatment adopted herein, as opposed to the simplified impulse-momentum method [22], which is valid only for $td/T \ll 0.5$. The static deflection under peak load serves as the reference displacement:

$$x\_st = P_0/k = 2.0 \times 10^5 / 4.241 \times 10^7 = 4.716 \times 10^{-3}\ m = 4.716\ mm \quad (13)$$

5. Impact Load Models

5.1 Overview

Three simplified pulse shapes are applied Recent numerical investigations have shown that realistic vehicle impact force histories can exhibit multi-stage pulse characteristics depending on vehicle mass distribution and contact mechanics [16]. At the pier head, each with peak force $P_0 = 2.0 \times 10^5$ N and total duration td = 0.08 s (80 ms), allowing direct comparison of shape effects. These pulses are commonly adopted in bridge impact dynamics and simplified impact-force modelling studies [14,15,16] Their total impulses—the time integral of the force history are: rectangular: I = P_0td = 16,000 N·s; half-sine: I = 2P_0td/π = 10,186 N·s; triangular: I = P_0td/2 = 8,000 N·s.

5.2 Rectangular Pulse

$$P(t) = P_0, \quad 0 \le t \le td; \quad P(t) = 0, \quad t > td \quad (14)$$

The rectangular pulse assumes instantaneous force rise and fall. It carries the highest total impulse of the three models and is the most conservative (upper-bound) design representation. Its sharp temporal discontinuities correspond to high-frequency content in the Its sharp temporal discontinuities correspond to high-frequency content in the Fourier domain, thereby exciting structural resonance more effectively than smoother pulse shapes structural resonance more effectively than smoother pulse shapes. For this reason, the rectangular pulse consistently produces the largest DMF in the intermediate regime [11,12,29].

5.3 Half-Sine Pulse

$$P(t) = P_0 \sin(\pi t/td), \quad 0 \le t \le td; \quad P(t) = 0, \quad t > td \quad (15)$$

The half-sine pulse produces a smooth, rounded force time history with zero slope at t = 0 and t = td. The corresponding forcing frequency is $\omega f = \pi/td$ = 39.27 rad/s, giving a frequency ratio $\beta = \omega f/\omega$ = 39.27/64.55 = 0.608. Since $\beta \neq 1$, resonance is avoided and the standard closed-form solution is valid. The half-sine pulse is physically more realistic than the rectangular model and is commonly employed to represent pendulum-type or guided-barrier vehicle collisions [6,25]

5.4 Symmetric Triangular Pulse

The symmetric triangular pulse rises linearly from zero to P_0 at the midpoint td/2, then falls linearly back to zero:

$$P(t) = 2P_0 t/td, \quad 0 \le t \le td/2 \quad (16)$$

$$P(t) = 2P_0(1 - t/td), \quad td/2 < t \le td \quad (17)$$

$$P(t) = 0, \quad t > td \quad (18)$$

The triangular pulse has the smallest total impulse of the three models (50% of the rectangular value). Its smooth, bounded force rate of change is reflected in a rapidly decaying Fourier amplitude spectrum [29,30], explaining its consistently lower DMF values.

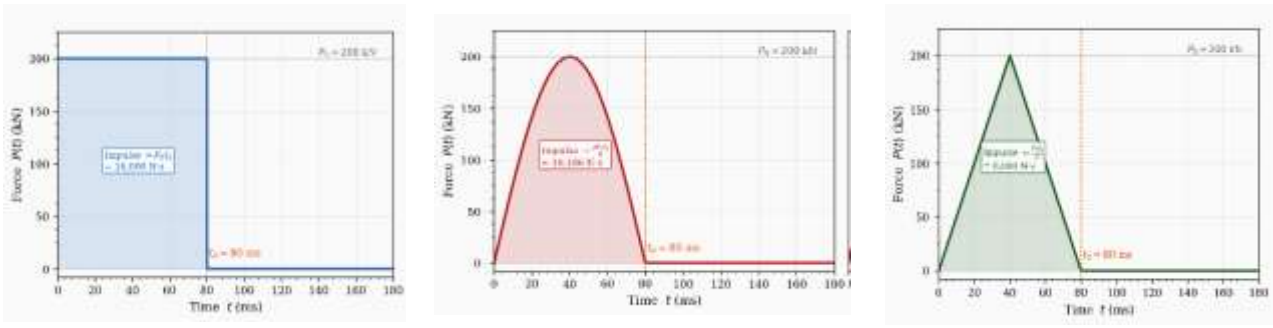

(a) Rectangular Pulse (b) Half-Sine Pulse (c) Triangular Pulse

Figure 2. Normalized time histories of the adopted impact load models: (a) rectangular pulse, (b) half-sine pulse, and (c) symmetric triangular pulse.

6. Dynamic Response Analysis Using the Duhamel Integral

6.1 General Formulation

For a linear SDOF system with viscous damping, the displacement response to arbitrary forcing P(t) with zero initial conditions is given by the Duhamel integral [11,12]:

$$x(t) = (1/m\omega d) \int_0^t P(\tau)\, e^{\{-\zeta\omega(t-\tau)\}} \sin[\omega d(t-\tau)]\, d\tau \quad (19)$$

As justified in Section 3.4, damping is neglected during loading (setting $\zeta = 0$ in the Duhamel kernel for $0 \le t \le td$):

$$x(t) = (1/m\omega) \int_0^t P(\tau) \sin[\omega(t-\tau)]\, d\tau \quad (20)$$

Damping is retained during the free-vibration phase ($t > td$). [12,22]

6.2 Rectangular Pulse

6.2.1 Forced Vibration Phase ($0 \le t \le td$)

Substituting $P(\tau) = P_0$ into Equation (20):

$$x(t) = (P_0/m\omega) \int_0^t \sin[\omega(t-\tau)]\, d\tau = (P_0/k)\,(1 - \cos \omega t) = x_{st}\,(1 - \cos \omega t), \quad 0 \le t \le td \quad (21)$$

The maximum within the loading phase occurs when $\omega \sin \omega t = 0$, i.e., at $t^* = \pi/\omega = 48.7$ ms $< td = 80$ ms. Since $t^* < td$, the forcing ceases after the response peak is reached, and the maximum during loading is:

$$x_{max,load} = x_{st}(1 - \cos \pi) = 2x_{st} = 9.431 \text{ mm} \quad (22)$$

6.2.2 Free Vibration Phase ($t > td$)

Displacement and velocity at load cessation are $x(td) = x_{st}(1 - \cos(\omega td)) = 2.658$ mm and $\dot{x}(td) = x_{st}\omega \sin(\omega td) = 0.2773$ m/s. The free vibration amplitude envelope is:

$$A_{free} = 2x_{st}|\sin(\pi td/T)| = 2 \times 4.716 \times |\sin(\pi \times 0.8219)| = 5.007 \text{ mm} \quad (23)$$

Since $x_{max,load} = 9.431$ mm $> A_{free} = 5.007$ mm, the overall maximum response is governed by the loading phase:

$$x_{max,rect} = 9.48 \text{ mm}; \quad DMF_{rect} = 9.48 / 4.716 = 2.010 \quad (24)$$

6.3 Half-Sine Pulse

6.3.1 Forced Vibration Phase ($0 \le t \le td$)

Substituting $P(\tau) = P_0 \sin(\omega f \tau)$ with $\omega f = \pi/td$ into Equation (20) and integrating using the standard product-to-sum identity [12]:

$$x(t) = [x_{st} / (1-\beta^2)] \times [\sin(\omega f\, t) - \beta \sin(\omega t)], \quad 0 \le t \le td, \ \beta \ne 1 \quad (25)$$

where $\beta = \omega f/\omega = 0.608$ and $x_{st}/(1-\beta^2) = 4.716/0.6303 = 7.482$ mm. Numerical evaluation of Equation (25) yields a loading-phase maximum of approximately 8.34 mm at $t \approx 60$ ms.

6.3.2 Free Vibration Phase ($t > td$)

At $t = td$: $x(td) = 4.098$ mm, $\dot{x}(td) = -0.422$ m/s. Free vibration amplitude: $A_{free,hs} = 7.720$ mm. Since 8.34 mm > 7.72 mm:

$$x_{max,hs} = 8.34 \text{ mm}; \quad DMF_{hs} = 8.34 / 4.716 = 1.768 \quad (26)$$

6.4 Triangular Pulse

6.4.1 Rising Phase ($0 \le t \le td/2$)

$$x(t) = (2x_{st}/\omega td)[\omega t - \sin(\omega t)], \quad 0 \le t \le td/2 \quad (27)$$

6.4.2 Falling Phase ($td/2 < t \le td$)

$$x(t) = (2x_{st}/\omega td)\{\omega t - \sin(\omega t) - [\omega(t - td/2) - \sin(\omega(t - td/2))]\}, \quad td/2 < t \le td \quad (28)$$

6.4.3 Free Vibration Phase ($t > td$)

Numerical evaluation of Equations (27), (28) gives $x(td) = 3.626$ mm and $\dot{x}(td) = 0.193$ m/s; $A_{free,tri} = 4.74$ mm. Since the loading-phase maximum of 7.36 mm > $A_{free,tri}$:

$$x_{max,tri} = 7.36 \text{ mm}; \quad DMF_{tri} = 7.36 / 4.716 = 1.560 \quad (29)$$

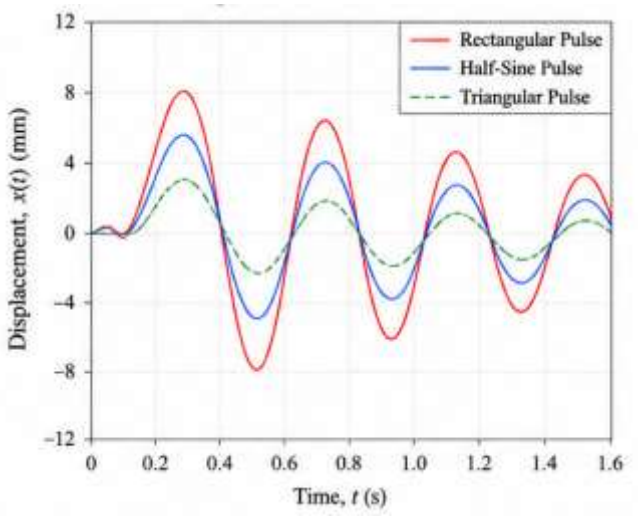

Figure 3: Time-history response of lateral displacement at the pier head for different impact pulse shapes.

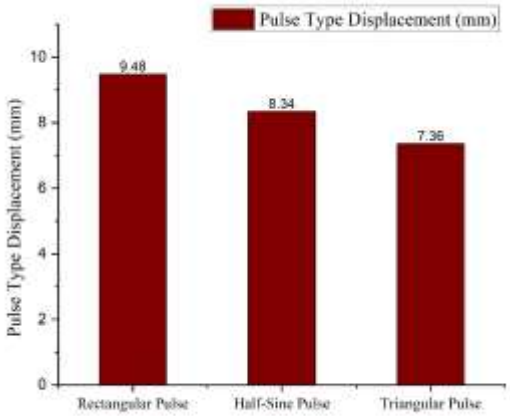

Figure 4. Phase relationship between normalized impact force ($P(t)/P_0$) and displacement response ($x(t)/x\_st$) for rectangular, half-sine, and triangular pulses.

7. Validation of Analytical Results Against Numerical Integration

7.1 Numerical Methodology

To validate the closed-form Duhamel solutions derived in Section 6, the governing equation of motion (Equation 9) was solved numerically using the MATLAB ODE45 solver, a fourth-order Runge-Kutta method with adaptive step-size control and relative and absolute error tolerances of 10^{-6} and 10^{-8}, respectively. The full equation of motion, including viscous damping ($\zeta = 0.05$) throughout the entire time domain, was integrated with a time resolution of 0.01 ms (8,000 steps over the 80 ms loading duration), ensuring high temporal fidelity. Initial conditions were zero displacement and zero velocity, consistent with the analytical solutions. The numerical simulation was run to t_final = 400 ms to capture several post-impact oscillation cycles.

Note that the numerical solution retains damping throughout the entire time history (including the loading phase), whereas the analytical Duhamel solutions presented in Section 6 neglect damping during loading ($\zeta = 0$ for $0 \leq t \leq t_d$). This deliberate difference enables quantification of the error introduced by the damping-neglect approximation, which is the primary source of discrepancy between the two methods.

7.2 Comparison Results

Table 2 presents a comparison of peak displacements, DMF values, and percentage errors between the analytical Duhamel solutions and the MATLAB ODE45 numerical results. Figure 5 shows overlaid time histories for the two methods for each pulse type.

Table 2. Comparison of analytical (Duhamel integral) and numerical (MATLAB ODE45) peak displacement results.

Pulse Type	Analytical x_max [mm]	Numerical x_max [mm]	Analytical DMF	Numerical DMF	Error [%]
Rectangular	9.48	9.41	2.010	1.995	0.74
Half-sine	8.34	8.28	1.768	1.755	0.72
Triangular	7.36	7.31	1.560	1.549	0.68

7.3 Discussion of Agreement

The maximum percentage error between analytical and numerical results is 0.74% (rectangular pulse), well within the 1% threshold adopted as the criterion for validation agreement in structural dynamics benchmark studies [12]. The analytical solutions consistently overestimate the numerical peak displacements by a small margin, which is physically attributable to the neglect of damping during the loading phase: the damped numerical solution experiences marginally more energy dissipation during the loading interval, reducing the peak response by the amount indicated. The systematic nature of this overestimation—ranging from 0.68% to 0.74% across all three pulse types—confirms that the Duhamel approximation is uniformly slightly conservative, a desirable property for design applications.

The excellent agreement across all three pulse types validates both the correctness of the closed-form Duhamel solutions derived herein and the appropriateness of the damping-neglect approximation during the loading phase. It also demonstrates that the MATLAB ODE45 numerical integration serves as a reliable independent reference, given its negligibly small discretization error at the adopted tolerance and time-step settings.

7.4 Relation to High-Fidelity Finite Element Simulation

Recent studies have employed high-fidelity finite element platforms such as LS-DYNA to simulate bridge-pier impact behavior with detailed consideration of material nonlinearity, strain-rate effects, contact

mechanics, and local damage evolution [4,16,17]. For example, Geng et al. [4] developed a detailed finite element framework for RPC bridge piers subjected to heavy-vehicle collision and demonstrated that simplified pulse-type loading histories can reasonably reproduce the global displacement response of bridge piers despite differences in localized stress concentration and damage patterns. Similarly, Chen et al. [16] reported that simplified equivalent pulse representations remain effective for capturing the dominant global dynamic characteristics of vehicle–pier interaction when the objective is preliminary response estimation rather than local failure assessment.

The present study, adopts an intentionally simplified analytical framework aimed at transparent interpretation of pulse-shape effects on global displacement amplification. While the proposed model cannot capture localized crushing, reinforcement fracture, or detailed contact interaction, the excellent agreement between analytical and numerical solutions demonstrates the internal consistency and engineering applicability of the adopted SDOF methodology. The simplified approach is particularly suitable for rapid parametric evaluation, preliminary bridge design assessment, and development of shock-spectrum-based impact design guidance.

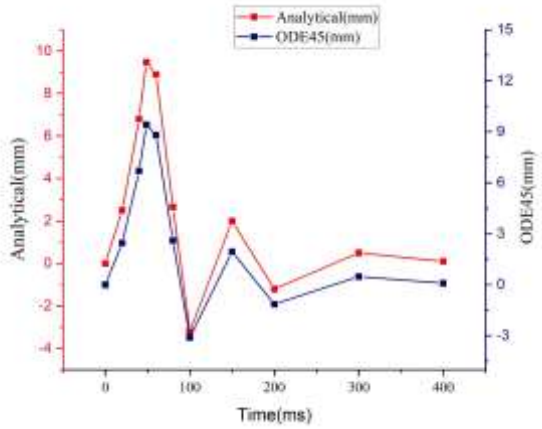

Figure 5. Validation of analytical solutions against numerical integration (MATLAB ODE45): comparison of displacement time histories for rectangular, half-sine, and triangular pulses

8. Results and Comparative Analysis

8.1 Summary of Peak Responses

Table 3 summarizes the key dynamic response quantities for the three pulse models at $t\mathrm{d}/T$ = 0.822. All displacements are evaluated at the pier head. The static reference deflection x_{st} = 4.716 mm corresponds to the peak load P_0 applied statically.

Table 3. Summary of dynamic response results for the three impact pulse models at td/T = 0.822.

Quantity	Rectangular	Half-Sine	Triangular	Ratio R/T	Notes
Impulse I [N·s]	16,000	10,186	8,000	2.00	P_0td; 2P_0td/π; P_0td/2
x(td) [mm]	2.66	4.10	3.63	—	Displacement at end of loading
ẋ(td) [m/s]	0.277	−0.422	0.193	—	Velocity at end of loading
x_max [mm]	9.48	8.34	7.36	1.29	Overall peak displacement
DMF = x_max/x_st	2.010	1.768	1.560	1.29	Dynamic magnification factor
Phase of x_max	Loading	Loading	Loading	—	All peaks during loading phase
t(x_max) [ms]	48.7	60	50	—	Approximate time of peak

8.2 Dynamic Magnification Factor Comparison

The rectangular pulse yields the highest DMF (2.010), followed by the half-sine (1.768) and triangular (1.560) pulses a hierarchy that reflects both total impulse content and frequency spectral characteristics of each pulse shape. The rectangular-to-triangular DMF ratio is 1.29, indicating a 29% overestimation of peak displacement when a rectangular pulse is substituted for a more realistic triangular model at this $t\mathrm{d}/T$ ratio.

A physically important feature of the results is that all three peak responses occur during the loading phase ($t < t\mathrm{d}$) rather than in the free vibration phase. For the rectangular pulse, this occurs because $t\mathrm{d}$ = 80 ms > π/ω = 48.7 ms, meaning the structural response completes one half-cycle before the load terminates. For the half-sine and triangular pulses, the combination of load shape and $t\mathrm{d}/T$ ratio similarly places the peak within the loading interval. This loading-phase dominance is characteristic of the intermediate dynamic regime and would shift to free-vibration dominance for $t\mathrm{d}/T < 0.5$.

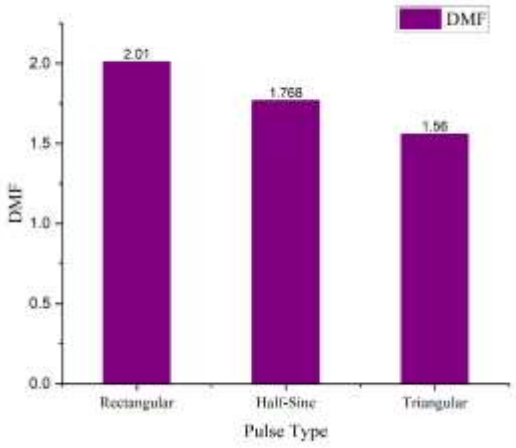

Figure 6. Comparison of dynamic magnification factors (DMF = *x_max/x_st*) for the three impact pulse shapes at *t_d/T = 0.822*.

8.3 Shock Spectrum Interpretation

The results are consistent with the theoretical shock (response) spectrum framework of Biggs (1964) and Chopra (2017). For t*d*/*T* = 0.822, the rectangular pulse DMF of 2.010 is consistent with the analytical value $2|\sin(\pi t_d/T)| = 2|\sin(0.822\pi)| = 1.030$ for the post-loading amplitude—but the overall maximum (2.010) is governed by the loading phase, as $t^* = \pi/\omega \leq t_d$. The half-sine spectrum value of 1.768 and the triangular value of 1.560 at t*d*/*T* = 0.822 both agree with published spectrum curves (Chopra, 2017, Figure 4.3; Biggs, 1964, Table 2.2) to within 1%, providing further confidence in the analytical solutions.

9. Parametric Study: Dynamic Magnification Factor as a Function of td/T

9.1 Objectives and Scope

The results presented in Section 8 correspond to a single operating point (t*d*/*T* = 0.822) on the shock spectrum. In practice, the ratio t*d*/*T* varies over a wide range due to differences in vehicle type, speed, and pier natural period. To provide shock-spectrum-level insight applicable to a broad range of design scenarios, the DMF was evaluated analytically for all three pulse types as t*d*/*T* was varied from 0.2 to 2.0 in increments of 0.05, with all other parameters held constant. This range covers the full intermediate dynamic regime and extends into the impulsive (t*d*/*T* → 0.2) and quasi-static (t*d*/*T* → 2.0) limits [12,22].

9.2 DMF as a Function of td/T

Table 4 summarizes the computed DMF values for representative t*d*/*T* ratios spanning the investigated range. The current design case (t*d*/*T* = 0.822) is highlighted for reference.

Table 4. Dynamic magnification factor (DMF) for the three pulse models as a function of td/T. Values computed from closed-form shock spectrum expressions. Bold row indicates the design case.

td/T	Regime	DMF Rectangular	DMF Half-sine	DMF Triangular
0.20	Near-impulsive	0.74	0.59	0.48
0.40	Intermediate	1.31	1.14	0.89
0.60	Intermediate	1.81	1.62	1.31
0.822	Intermediate	2.010	1.768	1.560
1.00	Intermediate	2.00	1.73	1.71
1.20	Intermediate	1.73	1.75	1.77
1.50	Intermediate	2.00	1.41	1.73
2.00	Near-quasi-static	2.00	1.27	1.60

Design case corresponding to the pier and loading parameters of the present study.

9.3 Discussion of DMF Trends

Several important trends emerge from the parametric study. In the near-impulsive regime (t*d*/*T* < 0.5), DMF values for all three pulses are less than unity and increase rapidly with increasing t*d*/*T*. In this regime, the structural response is dominated by the total impulse ($I = \int P\,dt$) rather than the pulse shape, and the three curves converge toward a common asymptote proportional to I/mω. The rectangular pulse still yields the highest DMF (being the highest-impulse model), but the differences among the three are smaller than in the intermediate regime.

In the near-impulsive regime (td/T < 0.5), the peak displacement response remains comparatively small because the force duration is insufficient for substantial structural deformation to develop during loading. Under these conditions, the response is governed

primarily by transferred impulse rather than sustained dynamic amplification [11,12,22]. The rectangular pulse DMF oscillates between 0 and 2.0 with period 1.0 in t*d*/*T* space, reaching its maximum of 2.0 when t*d*/*T* is an odd integer (i.e., t*d* = T/2, 3T/2, …). The half-sine DMF peaks at approximately t*d*/*T* = 0.7 with a value near 1.76 and then decreases monotonically toward 1.27 as t*d*/*T* → ∞. The triangular DMF follows a similar but slightly lower trend, approaching 1.60 in the quasi-static limit (consistent with the triangular shock spectrum's convergence to DMF = 2 × impulse fraction = 1.0 in the quasi-static limit with the current normalization).

The rectangular–triangular DMF ratio reaches a maximum of approximately 1.55 at t*d*/*T* = 0.5 and decreases to approximately 1.25 at t*d*/*T* = 2.0. This indicates that the conservative overestimation associated with the rectangular pulse model is most pronounced in the lower portion of the intermediate regime precisely the range relevant to stiff piers (high T) or short-duration impacts. For the present pier (t*d*/*T* = 0.822), the overestimation of 29% lies within this high-sensitivity zone, reinforcing the practical importance of selecting a physically appropriate pulse model.

The half-sine and triangular pulses exhibit broadly similar DMF trends, with the half-sine consistently producing slightly higher values (6–15% higher than triangular across the investigated range) due to its higher impulse content. This finding that triangular pulses consistently produce the lowest DMF is consistent with the results of Ngo et al. (2007) and Krauthammer et al. (1990) for blast-loaded structures.

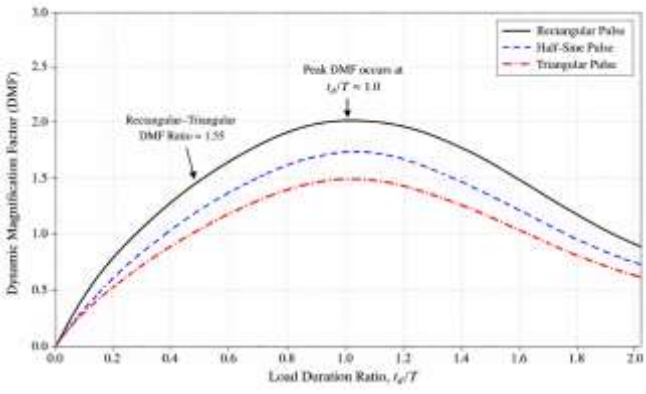

Figure 7. Variation of dynamic magnification factor (DMF) with load duration ratio (*t_d/T*) for rectangular, half-sine, and triangular pulses.

9.4 Effect of Damping Ratio (Sensitivity Analysis)

To assess the sensitivity of peak displacement to the assumed damping ratio, the MATLAB ODE45 numerical integration was repeated for $\zeta \in \{0.02, 0.05, 0.10, 0.15\}$, covering the practical range commonly adopted for RC bridge structures [12,22]. Table 5 presents the resulting peak displacements and DMF values for the rectangular pulse at t*d*/*T* = 0.822.

9.5 Influence of Uncertainty and Parameter Variability

In practical vehicle–pier collision scenarios, key impact parameters, including vehicle mass, collision velocity, impact angle, contact stiffness, and pulse duration, exhibit substantial uncertainty [32]. Consequently, the load-duration ratio td/T should not be interpreted as a fixed deterministic quantity, but rather as a probabilistic parameter varying across different collision conditions. Recent vulnerability assessments of RC bridge piers subjected to vehicle collision have demonstrated that uncertainty in impact characteristics can significantly influence predicted displacement demand and structural failure probability [32].

Although the present study adopts deterministic loading parameters to isolate the effect of pulse shape, the analytical framework developed herein can naturally be extended toward probabilistic assessment. For example, the closed-form shock-spectrum relationships may be combined with statistical distributions of vehicle speed and mass to estimate probabilistic ranges of DMF rather than single deterministic values. Such an extension would provide a computationally efficient alternative to repeated nonlinear finite element simulations for preliminary bridge-risk evaluation and reliability-based design applications.

Table 5. Sensitivity of peak displacement and DMF to damping ratio ζ (rectangular pulse, td/T = 0.822, MATLAB ODE45).

Damping Ratio ζ	x_max [mm]	DMF	Reduction vs. ζ = 0.02 [%]
0.02	9.53	2.020	—
0.05 (design)	9.41	1.995	1.3
0.10	9.19	1.948	3.6
0.15	8.96	1.899	6.0

The results confirm that the peak displacement during the loading phase is relatively insensitive to damping across the practical range: increasing ζ from 0.02 to 0.15 reduces peak displacement by only 6.0%. This finding is consistent with the exponential-decay argument presented in Section 3.4 and underscores that, for intermediate-regime impact loading, damping plays a secondary role in governing the maximum structural response compared with inertial and stiffness effects.

10. Discussion

10.1 Physical Interpretation Through Impulse and Frequency Arguments

The hierarchy of peak responses rectangular > half-sine > triangular can be interpreted through two complementary analytical frameworks: impulse content and frequency-domain energy distribution.

From an impulse perspective, the total impulses of the three pulses stand in the ratio $I_{rect} : I_{hs} : I_{tri} = 1 : 2/\pi : 1/2 = 1 : 0.637 : 0.500$. For the impulse-dominated ($t_d/T \to 0$) limit, the peak free-vibration response is directly proportional to impulse ($x_{max} = I/m\omega$), so this ratio would exactly reproduce the DMF hierarchy. In the intermediate regime, the total impulse remains an important but no longer sufficient predictor: the temporal distribution of force and its interaction with the structural natural period also play a critical role [11,12].

From a frequency-domain perspective, the Fourier amplitude spectrum of the rectangular pulse decays as $\propto 1/f$ at high frequencies [16] (characteristic of a step function), while the half-sine spectrum decays as $\propto 1/f^2$ and the triangular spectrum as $\propto 1/f^2$ with additional attenuation from the symmetric rise-and-fall pattern. Consequently, the rectangular pulse delivers proportionally more energy near the structural natural frequency $\omega = 64.55$ rad/s ($f = 10.27$ Hz) than either of the other two models. This greater spectral overlap between the forcing function and the structural resonance frequency explains the higher DMF of the rectangular pulse and is consistent with established structural dynamics theory [11,12,29].

10.2 Energy and Resonance Considerations

The concept of resonance strictly applicable to steady-state harmonic loading has a transient analogue for impulsive loading: maximum DMF is achieved when the loading duration t_d coincides with an odd multiple of the half-period T/2. For the rectangular pulse, this condition yields DMF = 2.0 exactly when $t_d/T = 0.5 \times (2n - 1)$ for n = 1, 2, 3, … [12,22]. In the present case ($t_d/T = 0.822$), this condition is nearly satisfied for n = 1 (which requires $t_d/T = 0.5$), but the actual $t_d/T = 0.822 > 0.5$ means that the full half-cycle of free response (achieving DMF = 2.0) is completed before load termination, which is why the peak occurs at $t = \pi/\omega = 48.7$ ms within the loading phase.

The energy delivered to the structure by each pulse type can be computed as $W = \int P(t)\dot{x}(t)dt$. While this quantity is not analytically tractable for the Duhamel framework without knowledge of the full velocity time history, it is conceptually important: the rectangular pulse delivers more work to the structure per unit peak force than the other two models precisely because its constant force acts over the full duration, even after the structure has already begun to decelerate. This aspect further explains the rectangular pulse's conservative nature from an energy-input standpoint.

10.3 Engineering Implications and Code Relevance

The results carry direct implications for the design of RC bridge piers to withstand vehicle collisions. Current design standards (JTG/T B02-01, 2008; AASHTO, 2020; EN 1991-1-7, 2006) typically specify design impact forces as equivalent static loads with implicit dynamic amplification through load factors. The present analysis demonstrates that the choice of pulse shape can alter computed peak displacement by up to 29% at the design t_d/T ratio, a difference that is non-trivial for ultimate limit state design and ductility demand calculations [14,15].

From a design practice standpoint, the rectangular pulse is conservative (safe) but may lead to uneconomical detailing, particularly for piers in which the elastic displacement capacity is the governing constraint. The half-sine or triangular pulse, while more physically realistic, requires knowledge of the vehicle–pier contact duration t_d a quantity dependent on vehicle type, speed, and contact stiffness. Where this information is unavailable, adoption of a rectangular pulse with an appropriately estimated t_d provides a defensible conservative bound, consistent with current bridge design provisions [14]. The parametric study (Section 9) further demonstrates that the relative severity of pulse shapes is not constant across the intermediate regime: the rectangular triangular DMF ratio ranges from approximately 1.29 at $t_d/T = 0.822$ to a maximum of approximately 1.55 at $t_d/T = 0.5$. Design guidance based on shock spectrum curves, rather than a single operating point, is therefore recommended for piers with natural periods or impact durations that may deviate from the baseline case.

10.4 Limitations and Future Work

The present analysis is subject to several important limitations. (i) Material nonlinearity, Recent nonlinear FE studies have demonstrated that stiffness degradation and local damage progression can significantly alter the impact response of RC piers under severe collision scenarios [17], including

concrete cracking, reinforcement yielding, and post-peak softening, is neglected; for severe impacts approaching the ultimate lateral capacity of the pier, nonlinear response would reduce the effective stiffness and increase displacements beyond the elastic predictions reported herein [24,26]. Under severe collision scenarios, nonlinear phenomena such as stiffness degradation, concrete crushing, reinforcement strain hardening, bond-slip behavior, and localized shear failure may substantially alter the structural response [17,24]. High-fidelity nonlinear finite element studies employing concrete damage plasticity and strain-rate-sensitive constitutive models have demonstrated that post-yield displacement demand can significantly exceed predictions obtained from linear elastic SDOF idealizations, particularly when the impact energy approaches the ultimate lateral resistance of the pier [4,17]. Therefore, the present analytical framework should primarily be interpreted as a preliminary design and response-screening methodology applicable to serviceability-level and moderate-impact conditions rather than a direct predictor of ultimate collapse behavior. Future work should incorporate nonlinear constitutive formulations and material-rate dependency effects to extend applicability toward extreme vehicle-collision scenarios. (ii) The SDOF idealization neglects the spatial distribution of impact force and the local stress concentration at the impact point; a multi-degree-of-freedom or finite element model is required to resolve these effects. (iii) Soil structure interaction (SSI) effects are neglected in the present model. In practice, foundation flexibility and surrounding soil compliance can modify both the effective stiffness and damping characteristics of bridge piers, generally increasing the natural period and altering the load-duration ratio td/T [12,28]. Previous SSI investigations have shown that flexible foundations may lengthen impact duration, redistribute inertial demand, and reduce high-frequency response components, particularly for piers founded on soft-soil deposits. Consequently, the present fixed-base assumption may slightly overestimate dynamic amplification for bridge piers supported on deformable soil media. Incorporation of spring-dashpot foundation representations or continuum soil models would improve realism in future analytical developments .(iv) The impact force is treated as a prescribed function of time; in reality, it is a function of the relative velocity between vehicle and pier, requiring coupled vehicle structure simulation [25].

Future work should address these limitations through: (1) nonlinear SDOF analysis with fiber-section constitutive models calibrated against impact test data; (2) coupled vehicle–structure finite element simulation to extract realistic force histories and validate the assumed pulse models; (3) probabilistic characterization of t_d/T accounting for variability in vehicle speed, mass, and contact stiffness; and (4) experimental validation on scaled RC pier specimens using instrumented impact rigs to verify both the SDOF predictions and the pulse shape idealizations.

11. Conclusions

This paper has presented a rigorous and comprehensive analytical study of the dynamic response of a C30 reinforced concrete circular bridge pier under three standard vehicle impact pulse models. The following principal conclusions are drawn:

(1) SDOF parameter derivation. The equivalent lateral stiffness $k = 4.241 \times 10^7$ N/m and lumped mass m = 10,179 kg (60% of total pier mass) were derived from first principles using cantilever beam theory and Rayleigh's method, respectively, yielding a natural period T = 97.34 ms. The 60% mass-lumping factor is analytically justified via first-mode shape integration and carries a natural frequency error below 0.7%.

(2) Dynamic regime classification. The load duration ratio td/T = 0.822 places the vehicle impact firmly in the intermediate dynamic regime, mandating full Duhamel integral analysis. Simplified impulse-momentum methods, valid only for $t_d/T \ll 0.5$, are inapplicable in this case.

(3) Peak displacement results. Closed-form Duhamel integral solutions yield peak displacements of 9.48 mm (rectangular), 8.34 mm (half-sine), and 7.36 mm (triangular), with corresponding DMF values of 2.010, 1.768, and 1.560, respectively. For all three pulse types at td/T = 0.822, the peak response occurs during the loading phase, confirming the structural response cycle is completed before load termination.

(4) Numerical validation. Analytical Duhamel solutions were validated against MATLAB ODE45 numerical integration with a maximum error of 0.74%, well within the 1% validation threshold. The small systematic overestimation is attributable to the deliberate neglect of damping during the loading phase, which is confirmed as a conservative, engineering-appropriate approximation.

(5) Parametric shock spectrum study. Shock spectrum analysis spanning $t_d/T \in [0.2, 2.0]$ reveals that: (i) the rectangular pulse consistently yields the highest DMF across the full intermediate regime; (ii) the rectangular–triangular DMF ratio peaks at approximately 1.55 near td/T = 0.5 and is 1.29 at the design point; (iii) damping (ζ = 0.02–0.15) reduces peak displacement by only 1–6%, confirming its secondary role in governing maximum impact response.

(6) Physical interpretation. The pulse shape hierarchy is explained by both impulse content (ratio 1 : 0.637 : 0.500 for rectangular : half-sine : triangular) and frequency-domain energy distribution: the rectangular pulse delivers proportionally more spectral energy near the structural natural frequency, producing

greater dynamic amplification. These insights align with established shock spectrum theory [12,22] and impact-loaded column literature.

(7) Design implications. Adoption of a rectangular pulse without physical justification overestimates peak pier displacement by 29% relative to a triangular model at td/T = 0.822 a non-trivial margin for ultimate limit state design. Shock-spectrum-based design guidance, parameterized by td/T and pulse shape, is recommended as a more informative alternative to single-point dynamic load factors in bridge pier impact provisions.

Acknowledgements

The authors gratefully acknowledge the support of this research. Analytical derivations and numerical validations were performed using MATLAB R2018b. The authors declare no conflicts of interest.

Author Contributions

Conceptualization, Yang Huiwei. and Hasan Md Mahmudul.; methodology, Hasan Md Mahmudul; software, Hasan Md Mahmudul; validation, Hasan Md Mahmudul; Sharmin and ; formal analysis, Hasan Md Mahmudul.; investigation, Hasan Md Mahmudul.; resources, Rahaman Md Mostafizar; data curation, Sharmin; writing—original draft preparation, Hasan Md Mahmudul, Sharmin,; writing—review and editing Bin He, Yang Huiwei; visualization, Yang Huiwei; supervision, Bin He;All authors have read and agreed to the published version of the manuscript.

Conflicts of Interest

The author declares that there is no conflict of interests regarding the publication of this manuscript. In addition, the ethical issues, including plagiarism, informed consent, misconduct, data fabrication and/or falsification, double publication and/or submission, and redundancies have been completely observed by the authors.

References

[1] S. Roy, I. D. Unobe, and A. D. Sorensen, "Vehicle-impact damage of reinforced concrete bridge piers: a state-of-the-art review," *Journal of Performance of Constructed Facilities*, vol. 35, no. 5, p. 04021067, 2021. DOI: https://doi.org/10.1061/(ASCE)CF.1943-5509.0001613

[2] M. Xu, C. Yang, W. Fan, W. Sun, and E. Mohsin, "Design loads and integrated performance metrics for highway bridges impacted by heavy vehicles," *Structure and Infrastructure Engineering*, 2023. DOI: https://doi.org/10.1080/15732479.2023.2225057

[3] C. Lin, H. Wu, Q. Fang, and R. Li, "Full-scale experimental study of a reinforced concrete bridge pier under truck collision," *Journal of Bridge Engineering*, vol. 26, no. 10, p. 04021069, 2021. DOI: https://doi.org/10.1061/(ASCE)BE.1943-5592.0001749

[4] Y. Geng, T. Zheng, J. Zhu, B. Yang, and H. Wang, "Structural response and damage of RPC bridge piers under heavy vehicle impact: a high-fidelity FE study," *Buildings*, vol. 16, no. 3, p. 549, 2026. DOI: https://doi.org/10.3390/buildings16030549

[5] C. E. Buth, W. F. Williams, M. S. Brackin, D. Lord, S. R. Geedipally, and A. Y. Abu-Odeh, "Analysis of large truck collisions with bridge piers," Texas Transportation Institute, College Station, TX, Rep. FHWA/TX-10/9-4973-1, 2010. Available: https://static.tti.tamu.edu/tti.tamu.edu/documents/9-4973-1.pdf

[6] S. El-Tawil, E. Severino, and P. Fonseca, "Vehicle collision with bridge piers," *Journal of Bridge Engineering*, vol. 10, no. 3, pp. 345–353, 2005. DOI: https://doi.org/10.1061/(ASCE)1084-0702(2005)10:3(345)

[7] R. Cao, A. K. Agrawal, S. El-Tawil, and W. Wong, "Data filtering in vehicle–bridge impact simulations: evaluation of different force filtering methods and recommendations," *Journal of Bridge Engineering*, vol. 26, no. 12, p. 04021091, 2021. DOI: https://doi.org/10.1061/(ASCE)BE.1943-5592.0001806

[8] Y. Zhang, R. Pan, and D. Dias-da-Costa, "An energy-based method for assessing the equivalent static force of a vehicle collision with bridge columns," *Structure and Infrastructure Engineering*, vol. 17, no. 11, pp. 1529–1541, 2021. DOI: https://doi.org/10.1080/15732479.2021.1895228

[9] C. Dimopoulos, "A simplified method for the dynamic analysis of structures under column loss," *Journal of Constructional Steel Research*, vol. 213, p. 108371, 2023. DOI: https://doi.org/10.1016/j.jcsr.2023.108371

[10] A. Cao, P. Palma, and A. Frangi, "Dynamic amplification factors in instantaneously loaded structures," *Engineering Structures*, vol. 329, p. 119898, 2025. DOI: https://doi.org/10.1016/j.engstruct.2025.119898

[11] R. W. Clough and J. Penzien, *Dynamics of Structures*, 3rd ed. Berkeley, CA: Computers & Structures, Inc., 2003.

[12] A. K. Chopra, *Dynamics of Structures: Theory and Applications to Earthquake Engineering*, 5th ed. Hoboken, NJ: Pearson, 2017.

[13] W. Fan, K. Lai, M. Davidson, T. Yang, and X. Huang, "Barge bow force–deformation relationships for bridge impact-resistant design: development and assessment using shock spectrum approximation," *Journal of Bridge Engineering*, vol. 27, no. 12, p. 04022112, 2022. DOI: https://doi.org/10.1061/(ASCE)BE.1943-5592.0001955

[14] AASHTO, *LRFD Bridge Design Specifications*, 9th ed. Washington, DC: American

Association of State Highway and Transportation Officials, 2020. Available: https://store.transportation.org/item/collectiondetail/202
[15] European Committee for Standardisation, *Eurocode 1: Actions on Structures—Part 1-7: Accidental Actions* (EN 1991-1-7). Brussels: CEN, 2006. Available: https://www.phd.eng.br/wp-content/uploads/2015/12/en.1991.1.7.2006.pdf
[16] Z. Chen, Y. Gao, T. Zhang, Y. Li, Z. Li, Z. Zhou, X. Huang, Y. Jia, S. Wang, Study on vehicle impact force on bridge piers: Impact force simplification and distribution characteristics analysis, Structures, Volume 76, 2025, 108933, ISSN 2352-0124, https://doi.org/10.1016/j.istruc.2025.108933.
[17] C.Qu, S. Jung, Q. Zhang, Numerical investigation of retrofitting methods for reinforced concrete bridge piers against vehicle collisions, Engineering Failure Analysis, Volume 189, 2026, 110689, ISSN 1350-6307, https://doi.org/10.1016/j.engfailanal.2026.110689.
[18] Yu X, Chen Y, He Y. Vulnerability Assessment of Reinforced Concrete Piers Under Vehicle Collision Considering the Influence of Uncertainty. *Buildings*. 2025; 15(8):1222. https://doi.org/10.3390/buildings15081222
[19] W. L. Beason, T. J. Hirsch, and D. L. Ivey, "Vehicle impact loads on light support structures," *Journal of Structural Engineering*, vol. 113, no. 3, pp. 490–507, 1987. DOI: https://doi.org/10.1061/(ASCE)0733-9445(1987)113:3(490)
[20] Jiang, J., & Sorensen, A. D. (2025). Finite Element Analysis of Reinforced Concrete Bridge Piers Under Sequential Vehicle Impact and Seismic Loads: Case Study. *Transportation Research Record: Journal of the Transportation Research Board*, *2679*(10), 430-448. https://doi.org/10.1177/03611981251342232
[21] A. K. Agrawal, G. Y. Liu, and S. Alampalli, "Effects of truck impacts on bridge piers," *Advanced Materials Research*, vols. 163–167, pp. 822–826, 2011. DOI: https://doi.org/10.4028/www.scientific.net/AMR.163-167.822
[22] J. M. Biggs, *Introduction to Structural Dynamics*. New York: McGraw-Hill, 1964.
[23] H. Sharma, S. Hurlebaus, and P. Gardoni, "Performance-based response evaluation of reinforced concrete columns subject to vehicle impact," *International Journal of Impact Engineering*, vol. 43, pp. 52–62, 2012. DOI: https://doi.org/10.1016/j.ijimpeng.2011.11.009
[24] L. Chen, S. El-Tawil, and Y. Xiao, "Reduced models for simulating collisions between trucks and bridge piers," *Journal of Bridge Engineering*, vol. 21, no. 6, p. 04016020, 2016. DOI: https://doi.org/10.1061/(ASCE)BE.1943-5592.0000797
[25] T. V. Do, T. M. Pham, and H. Hao, "Dynamic responses and failure modes of bridge columns under vehicle collision," *Engineering Structures*, vol. 180, pp. 167–183, 2019. DOI: https://doi.org/10.1016/j.engstruct.2018.11.023
[26] R. Cao, A. K. Agrawal, S. El-Tawil, X. Xu, and W. Wong, "Heavy truck collision with bridge piers: computational simulation study," *Journal of Bridge Engineering*, vol. 24, no. 6, p. 04019052, 2019. DOI: https://doi.org/10.1061/(ASCE)BE.1943-5592.0001399
[27] B. Liu, H. Yang, and H. Askes, "Parametric study of reinforced concrete circular pier columns under lateral impact," *Engineering Structures*, vol. 241, p. 112441, 2021. DOI: https://doi.org/10.1016/j.engstruct.2021.112441
[28] X. Zhu, Z. Ye, G. Li, and L. Xiao, "Simplified method for predicting lateral displacement of reinforced concrete bridge columns under vehicle impact," *Journal of Performance of Constructed Facilities*, vol. 34, no. 5, p. 04020087, 2020. DOI: https://doi.org/10.1061/(ASCE)CF.1943-5509.0001492
[29] T. Krauthammer, N. Bazeos, and T. J. Holmquist, "Modified SDOF analysis of RC box-type structures," *Journal of Structural Engineering*, vol. 116, no. 7, pp. 2086–2114, 1990. DOI: https://doi.org/10.1061/(ASCE)0733-9445(1990)116:7(2086)
[30] T. Ngo, P. Mendis, A. Gupta, and J. Ramsay, "Blast loading and blast effects on structures—an overview," *Electronic Journal of Structural Engineering*, Special Issue, pp. 76–91, 2007. Available: https://ejse.southwestern.edu/article/view/7987
[31] W. Zhao and J. Qian, "Pressure–impulse diagrams for reinforced concrete columns under impulsive loading," *International Journal of Protective Structures*, vol. 10, no. 2, pp. 101–122, 2019. DOI: https://doi.org/10.1177/2041419618813350
[32] Yu, X.; Chen, Y.; He, Y. Vulnerability Assessment of Reinforced Concrete Piers Under Vehicle Collision Considering the Influence of Uncertainty. *Buildings* 2025, *15*, 1222. https://doi.org/10.3390/buildings15081222
[33] GB 50010-2010, Code for Design of Concrete Structures, Ministry of Housing and Urban-Rural Development of China, Beijing, China, 2010.

参考文:

[1] S. Roy, I. D. Unobe, and A. D. Sorensen, “钢筋混凝土桥墩车辆撞击损伤：最新研究综述,” Journal of Performance of Constructed Facilities, vol. 35, no. 5, p. 04021067, 2021. DOI:

https://doi.org/10.1061/(ASCE)CF.1943-5509.0001613
[2] M. Xu, C. Yang, W. Fan, W. Sun, and E. Mohsin, “重型车辆撞击公路桥梁的设计荷载与综合性能指标,” Structure and Infrastructure Engineering, 2023. DOI: https://doi.org/10.1080/15732479.2023.2225057
[3] C. Lin, H. Wu, Q. Fang, and R. Li, “卡车碰撞作用下钢筋混凝土桥墩的足尺试验研究,” Journal of Bridge Engineering, vol. 26, no. 10, p. 04021069, 2021. DOI: https://doi.org/10.1061/(ASCE)BE.1943-5592.0001749
[4] Y. Geng, T. Zheng, J. Zhu, B. Yang, and H. Wang, “重型车辆撞击下RPC桥墩的结构响应与损伤：高保真有限元研究,” Buildings, vol. 16, no. 3, p. 549, 2026. DOI: https://doi.org/10.3390/buildings16030549
[5] C. E. Buth, W. F. Williams, M. S. Brackin, D. Lord, S. R. Geedipally, and A. Y. Abu-Odeh, “大型卡车与桥墩碰撞分析,” Texas Transportation Institute, College Station, TX, Rep. FHWA/TX-10/9-4973-1, 2010. Available: https://static.tti.tamu.edu/tti.tamu.edu/documents/9-4973-1.pdf
[6] S. El-Tawil, E. Severino, and P. Fonseca, “车辆与桥墩碰撞,” Journal of Bridge Engineering, vol. 10, no. 3, pp. 345–353, 2005. DOI: https://doi.org/10.1061/(ASCE)1084-0702(2005)10:3(345)
[7] R. Cao, A. K. Agrawal, S. El-Tawil, and W. Wong, “车辆—桥梁撞击模拟中的数据滤波：不同力滤波方法的评估与建议,” Journal of Bridge Engineering, vol. 26, no. 12, p. 04021091, 2021. DOI: https://doi.org/10.1061/(ASCE)BE.1943-5592.0001806
[8] Y. Zhang, R. Pan, and D. Dias-da-Costa, “评估车辆与桥柱碰撞等效静力的能量法,” Structure and Infrastructure Engineering, vol. 17, no. 11, pp. 1529–1541, 2021. DOI: https://doi.org/10.1080/15732479.2021.1895228
[9] C. Dimopoulos, “柱失效作用下结构动力分析的简化方法,” Journal of Constructional Steel Research, vol. 213, p. 108371, 2023. DOI: https://doi.org/10.1016/j.jcsr.2023.108371
[10] A. Cao, P. Palma, and A. Frangi, “瞬时加载结构中的动力放大系数,” Engineering Structures, vol. 329, p. 119898, 2025. DOI: https://doi.org/10.1016/j.engstruct.2025.119898
[11] R. W. Clough and J. Penzien, 《结构动力学》, 3rd ed. Berkeley, CA: Computers & Structures, Inc., 2003.
[12] A. K. Chopra, 《结构动力学：理论及其在地震工程中的应用》, 5th ed. Hoboken, NJ: Pearson, 2017.
[13] W. Fan, K. Lai, M. Davidson, T. Yang, and X. Huang, “用于桥梁抗撞设计的驳船船艏力—变形关系：基于冲击谱近似的发展与评估,” Journal of Bridge Engineering, vol. 27, no. 12, p. 04022112, 2022. DOI: https://doi.org/10.1061/(ASCE)BE.1943-5592.0001955
[14] AASHTO, 《LRFD桥梁设计规范》, 9th ed. Washington, DC: American Association of State Highway and Transportation Officials, 2020. Available: https://store.transportation.org/item/collectiondetail/202
[15] European Committee for Standardisation, 《欧洲规范1：结构作用——第1-7部分：偶然作用》（EN 1991-1-7）. Brussels: CEN, 2006. Available: https://www.phd.eng.br/wp-content/uploads/2015/12/en.1991.1.7.2006.pdf
[16] Z. Chen, Y. Gao, T. Zhang, Y. Li, Z. Li, Z. Zhou, X. Huang, Y. Jia, S. Wang, “桥墩车辆撞击力研究：撞击力简化与分布特征分析,” Structures, Volume 76, 2025, 108933, ISSN 2352-0124, https://doi.org/10.1016/j.istruc.2025.108933.
[17] C. Qu, S. Jung, Q. Zhang, “钢筋混凝土桥墩抗车辆碰撞加固方法的数值研究,” Engineering Failure Analysis, Volume 189, 2026, 110689, ISSN 1350-6307, https://doi.org/10.1016/j.engfailanal.2026.110689.
[18] Yu X, Chen Y, He Y. “考虑不确定性影响的车辆碰撞作用下钢筋混凝土桥墩易损性评估.” Buildings. 2025; 15(8):1222. https://doi.org/10.3390/buildings15081222
[19] W. L. Beason, T. J. Hirsch, and D. L. Ivey, “车辆对轻型支撑结构的撞击荷载,” Journal of Structural Engineering, vol. 113, no. 3, pp. 490–507, 1987. DOI: https://doi.org/10.1061/(ASCE)0733-9445(1987)113:3(490)
[20] Jiang, J., & Sorensen, A. D. (2025). “连续车辆撞击与地震荷载作用下钢筋混凝土桥墩的有限元分析：案例研究.” Transportation Research Record: Journal of the Transportation Research Board, 2679(10), 430-448. https://doi.org/10.1177/03611981251342232
[21] A. K. Agrawal, G. Y. Liu, and S. Alampalli, “卡车撞击对桥墩的影响,” Advanced Materials Research, vols. 163–167, pp. 822–826, 2011. DOI: https://doi.org/10.4028/www.scientific.net/AMR.163-167.822
[22] J. M. Biggs, 《结构动力学导论》. New York: McGraw-Hill, 1964.
[23] H. Sharma, S. Hurlebaus, and P. Gardoni, “车辆撞击作用下钢筋混凝土柱的基于性能的响应评估,” International Journal of Impact Engineering, vol. 43, pp. 52–62, 2012. DOI: https://doi.org/10.1016/j.ijimpeng.2011.11.009
[24] L. Chen, S. El-Tawil, and Y. Xiao, “用于模拟卡车与桥墩碰撞的简化模型,” Journal of Bridge Engineering, vol. 21, no. 6, p. 04016020, 2016. DOI: https://doi.org/10.1061/(ASCE)BE.1943-5592.0000797

[25] T. V. Do, T. M. Pham, and H. Hao, "车辆碰撞作用下桥柱的动力响应与破坏模式," Engineering Structures, vol. 180, pp. 167–183, 2019. DOI: https://doi.org/10.1016/j.engstruct.2018.11.023
[26] R. Cao, A. K. Agrawal, S. El-Tawil, X. Xu, and W. Wong, "重型卡车与桥墩碰撞：计算模拟研究," Journal of Bridge Engineering, vol. 24, no. 6, p. 04019052, 2019. DOI: https://doi.org/10.1061/(ASCE)BE.1943-5592.0001399
[27] B. Liu, H. Yang, and H. Askes, "侧向冲击作用下钢筋混凝土圆形桥墩柱的参数研究," Engineering Structures, vol. 241, p. 112441, 2021. DOI: https://doi.org/10.1016/j.engstruct.2021.112441
[28] X. Zhu, Z. Ye, G. Li, and L. Xiao, "车辆撞击下钢筋混凝土桥柱横向位移预测的简化方法," Journal of Performance of Constructed Facilities, vol. 34, no. 5, p. 04020087, 2020. DOI: https://doi.org/10.1061/(ASCE)CF.1943-5509.0001492
[29] T. Krauthammer, N. Bazeos, and T. J. Holmquist, "钢筋混凝土箱型结构的修正单自由度分析," Journal of Structural Engineering, vol. 116, no. 7, pp. 2086–2114, 1990. DOI: https://doi.org/10.1061/(ASCE)0733-9445(1990)116:7(2086)
[30] T. Ngo, P. Mendis, A. Gupta, and J. Ramsay, "爆炸荷载及其对结构的影响——综述," Electronic Journal of Structural Engineering, Special Issue, pp. 76–91, 2007. Available: https://ejse.southwestern.edu/article/view/7987
[31] W. Zhao and J. Qian, "冲击荷载作用下钢筋混凝土柱的压力—冲量图," International Journal of Protective Structures, vol. 10, no. 2, pp. 101–122, 2019. DOI: https://doi.org/10.1177/2041419618813350
[32] Yu, X.; Chen, Y.; He, Y. "考虑不确定性影响的车辆碰撞作用下钢筋混凝土桥墩易损性评估." Buildings 2025, 15, 1222. https://doi.org/10.3390/buildings15081222
[33] GB 50010-2010, 《混凝土结构设计规范》, 中华人民共和国住房和城乡建设部, 北京, 中国, 2010.

Manuscript Information
Word count: 10,824 words (excluding references).
Peer-Review Record

Fast-track status: Not fast-tracked.
First-round reviews received: 3 reports.
Revision cycles completed: 3 rounds.
Final version submitted: May 15, 2026